

The UV–mid-IR Spectral Energy Distribution of a $z = 1.7$ Quasar Host Galaxy

N.R. Ross¹, R.J. Assef¹, C.S. Kochanek^{1,2}, E. Falco³, S.D. Poindexter¹

ABSTRACT

We have measured the spectral energy distribution (SED) of the host galaxy of the $z_s = 1.7$ gravitationally lensed quasar SDSS J1004+4112 from $0.44 - 8.0 \mu\text{m}$ ($0.16 - 3.0 \mu\text{m}$ in the rest frame). The large angular extent of the lensed images and their separation from the central galaxy of this cluster lens allows the images to be resolved even with the Spitzer Space Telescope. Based on the SED, the host galaxy is a mixture of relatively old and intermediate age stars with an inferred stellar mass of $\log(M_\star/M_\odot) = 11.09 \pm 0.28$ and a star formation rate of $\log(\dot{M}/M_\odot \text{ yr}^{-1}) = 1.21 \pm 0.26$. Given the estimated black hole mass of $M_{BH} \simeq 10^{8.6} M_\odot$ from locally-calibrated correlations of black hole masses with line widths and luminosities, the black hole represents a fraction $\log(M_{BH}/M_\star) = -2.49 \pm 0.28$ of the stellar mass and it is radiating at 0.24 ± 0.05 of the Eddington limit. The ratio of the host stellar mass to the black hole mass is only marginally consistent with the locally observed ratio.

Subject headings: Quasar; Host galaxy; Gravitational lensing; Evolution; Super-massive black hole

1. Introduction

In the local universe, the host galaxies of active, luminous black holes tend to be bluer star forming galaxies with a roughly 1000:1 ratio between star formation and accretion rates (Kauffmann & Heckman 2005). More luminous AGN also show younger stellar populations.

¹Department of Astronomy, The Ohio State University, 140 W. 18th Ave., Columbus, OH 43210

²Center for Cosmology and Astroparticle Physics, The Ohio State University, 191 W. Woodruff Avenue, Columbus, OH 43210

³Harvard-Smithsonian Center for Astrophysics, 60 Garden Street, Cambridge, MA 02138

Moreover, the relative growth rates match the observed local ratio of stellar to black hole mass (Kauffmann & Heckman 2005; Marconi & Hunt 2003). At higher redshifts, $z > 1$, the picture is less clear because the greater distances and higher typical AGN luminosities make it increasingly difficult to study host galaxies. Studies by Peng et al. (2006a,b) argue that the relationship is shifted and that at this epoch ($z > 1$) the black hole mass grows faster relative to the stellar mass than is observed locally, while Lauer et al. (2007) and Di Matteo et al. (2008) argue for little change.

There is also considerable interest in the star formation rates of the hosts at these redshifts. With the now prevalent view that the black holes and stars grow in a self-regulating process (e.g. Hopkins et al. 2005a,b, 2006; Sijacki et al. 2007; Di Matteo et al. 2008), particularly during major mergers, it is of considerable importance to be able to estimate both the stellar mass and the star formation rate. In the Hopkins et al. (2005a,b) scenario, the peak star formation rates precede the peak quasar luminosity, and the quasar phase lasts about 10^7 years. Unfortunately, estimating both stellar masses and star formation rates at these redshifts requires not only a detection of the host but a reasonably complete spectral energy distribution (SED).

Here we make use of gravitational lensing to measure the SED of a $z_s = 1.73$ quasar host galaxy from $0.44\text{--}8.0\mu\text{m}$ and infer its mass and star formation rate. As emphasized by Peng et al. (2006b), quasar lenses are ideal laboratories for studies of quasar hosts because the lens magnification “pulls” the host out from under the quasar to provide a $\sim 10^2$ improvement in contrast. Moreover, the arced shapes of the lensed hosts are easily distinguished from PSF artifacts. Our target is the five image lens SDSS J1004+4112 (Inada et al. 2003, 2005; Sharon et al. 2005; Ota et al. 2006; Fohlmeister et al. 2007, 2008; Inada et al. 2008). This lens is created by a $z_l = 0.68$ cluster of galaxies (Inada et al. 2003), giving it exceptionally large image separations (a ~ 14 arcsec Einstein ring diameter) that both lead to very large images of the host and places the quasar images well away from the lens galaxy emission. In fact, the host is so extended and well-separated from the lens that it can be resolved by the Spitzer Space Telescope with relative ease. There are also additional, higher redshift lensed galaxies (Sharon et al. 2005) and time delay measurements between the various lensed images of the quasar of $\Delta\tau_{BA} = 40.6 \pm 1.8$ days, $\Delta\tau_{CA} = 821.6 \pm 2.1$ days, and $\Delta\tau_{AD} > 1250$ days (Fohlmeister et al. 2008). In §2 we describe how we measure the spectral energy distribution (SED) of the host galaxy and the quasar. In §3 we use these estimates to determine the luminosity, stellar mass, and star formation rate of the host galaxy. We assume a flat, $\Omega_0 = 0.3$, $H_0 = 70$ km/s/Mpc cosmology.

2. Data

We use Hubble Space Telescope (HST) and Spitzer Space Telescope (SST) observations of SDSS J1004+4112 in 8 bands covering the visual to mid-infrared wavelengths. The HST data consists of ACS/WFC B(F435W), V(F555W), I(F814W) observations and NICMOS/NIC2 H(F160W) observations. The SST/IRAC data consists of 3.6, 4.5, 5.8, and 8.0 μ m observations. For the V, I, H, and IRAC bands we have multiple observational epochs. A summary of the observations is given in Table 1. Each HST observation consists of several (typically 4) sub-exposures, drizzled together (Fruchter et al. 2002) to create one background-subtracted image. Each IRAC epoch consists of 36 dithered 96.8 second images in each of the IRAC channels. Starting with the Basic Calibrated Data frames, the mosaic is oversampled by a factor of 4 using MOPEX (Mosaicking and Point Source Extraction), with outlier rejection to remove cosmic rays. Typical image depths (in Vega magnitudes) are given in Table 1.

We first used a parametric model to fit the images using a combination of point sources for the quasars, exponential disks and de Vaucouleurs models for the cluster galaxies and Gaussians for the images of the host galaxies, all convolved with point spread function (PSF) models, as in Lehár et al. (2000). These have problems for estimating the flux of the host galaxy due to the fact that the PSF, generated by TinyTim for the HST bands and obtained from SST for the IRAC bands, has significant fractional errors at the peak of the quasar, exactly where the model for the host galaxy also peaks. The parametric models tend to overestimate the flux of the host galaxy in order to reduce the residuals at the position of the quasar. We will use these models only to correct aperture magnitudes for the effects of the point spread function.

We next created a series of masks which isolate regions on the images where the flux is dominated by either the host galaxy or the quasar, in both cases excluding flux from objects in the field. These masks have regions with value either 0 or 1 in order to exclude or include flux, respectively, in specific pixels when multiplied into the original images. We keep the masks consistent across all bands by geometrically transforming a master copy to the appropriate centering, pixel scale, and orientation of each observation. We defined three types of masks. Host masks exclude flux both near the quasars and away from the host images seen in the I/H data. Quasar masks include only flux near the peak of the quasar images. Background masks include a region outside the host mask which we use to estimate any residual background flux. Joint masks combine the host and the quasar masks to estimate the total flux of both components. Figure 1 superposes these masks on an H-band image.

When we apply a mask to a region, we calculate the flux f_{mask} under the mask. This flux

is a combination of the true flux in the masked region f with contamination f_{cont} spread into the masked region by the PSF, losses f_{loss} out of the region due to the PSF, and f_{back} due to any mis-estimation of the background during the image reduction process. For example, we estimate f_{cont} and f_{loss} for our host mask as follows. We start from the model of the image without PSF convolution. We then mask this image, convolve it with the PSF, and measure the flux under the second mask. Thus the contamination, f_{cont} , of the host mask region due to the PSF spreading flux out of the quasar mask region, is found by first masking the unconvolved model image with the quasar mask, convolving this masked image with the PSF, and then measuring the flux found in the host mask region, while f_{loss} is found by masking with the host mask, convolving with the PSF and then measuring the flux outside of the host mask. Since these corrections are modest, we are not very sensitive to the problems in the model image. We estimate the background by subtracting the model from the data and measuring the residuals in the background mask. The resulting flux for any region is then

$$f = f_{mask} - f_{cont} + f_{loss} - f_{back} \quad (1)$$

The measurements are summarized in Table 2. We first estimate statistical uncertainties in the magnitudes using a bootstrap resampling of the images. The bootstrap resampling technique creates an ensemble of trial images by sampling with replacement from the sub-images (dithers, CR Splits, etc.) that were averaged together for each observation. We analyze each trial image in the same manner as the true images and estimate error bars from the variance of the results over the trials. The remaining uncertainty arises from the background subtraction. We recompute all the estimates using two different regions for estimating the background flux, as well as a background estimate generated by the model fits. The dispersion of these background estimates, multiplied by the number of pixels in a given mask region, gives an estimate of the background uncertainties in each mask region. Small changes in the estimated background can have significant effects on the flux measured for the host because of the large number of pixels in both the host mask and the joint mask. The uncertainties we present in Table 2 are a combination of these statistical and background uncertainties, added in quadrature.

We use data from the ongoing monitoring of SDSS J1004+4112 (Fohlmeister et al. 2008) to correct for time variability of the quasar in the QSO and joint masks. We chose 13 December 2005 as the reference date, as many of our observations were made close to this date (see Table 1). We estimate the time delay corrections by comparing the flux measured in the monitoring project on or within ~ 2 days of the observation with the flux measured in the monitoring project on or within ~ 2 days of the reference date. These time delay corrections range from about 0.05 to -0.44 magnitudes. We use these time delay corrections only for the optical to near-IR observations of the quasar because the observations in the mid-IR show much less variability, as one would expect from the general trend of reduced

variability at longer wavelengths (e.g. Vanden Berk et al. 2004). We do not correct for the time delays between the lensed images because the image D time delay is not known (see Fohlmeister et al. 2008). Essentially, we will “time average” the properties of the quasar in our final results.

3. Analysis

We used an extended version of the SED template models presented by Assef et al. (2008) to fit the data for each lensed image. These templates consist of early-type, Sbc, Irr and QSO templates empirically derived by fitting the GALEX UV through SST/MIPS $24\mu\text{m}$ SEDs of 13623 “pure” galaxies (with no obvious signatures of nuclear activity) and 4242 quasars and galaxies with AGN activity in the NDWFS Boötes field (Jannuzi & Dey 1999), with redshifts measured by the AGN and Galaxy Evolution Survey (AGES, Kochanek et al. in prep.). Assef et al. (2008) details the procedure used to derive these templates, and they will be discussed in depth in an upcoming paper by Assef et al. (2009). A fit is produced by multiplying each template by a coefficient and finding the χ^2 minimizing fit to the data over these coefficients, with the added constraint that all template coefficients must be non-negative, as subtracting a template is unphysical (see the discussion in Assef et al. 2008, 2009).

For images A, B, and C we separately fit the host, QSO and joint SEDs, while for image D we only fit the joint SED. Figures 2, 3, and 4 show examples of the template fits and Table 3 lists the host luminosities derived from the template fits to the host, QSO, and joint mask data. These luminosities are corrected for magnification by the lens using magnifications of 28.5, 19.1, 9.8, 7.8 for the A, B, C, and D images, respectively, from the models of Inada et al. (2008; Oguri, private communication).

We used several methods to estimate our systematic uncertainties in determining the properties of the host galaxy. First, we fit the host mask data both with and without the B-, V-, and I-band data in order to examine whether eliminating the data points with the worst signal-to-noise ratios would produce any difference in the fits. These fits produced significant variations on an image by image basis, but showed little effect on the averages, which is unsurprising, considering that these data points are already heavily downweighted by their large uncertainties during the fitting process. Next we fit the QSO and joint mask data once by allowing all template components to vary and once by fixing the ratios of the galaxy templates using the results of the host mask fits. These fits produced different results for the template ratios (although the Irr template was never favored) and the joint fits have systematically brighter host and fainter AGN components than the simple sum of

the separate host and quasar mask results, but these variations had no significant effect on the luminosities, masses, or star formation rates.

We use the template fits and standard scaling relations to estimate the stellar mass and star formation rate of the host galaxy. We use the estimated rest frame $8.0\mu\text{m}$ flux of the host to estimate the total infrared luminosity based on the scalings of Bavouzet et al. (2008), which in turn is used to estimate the obscured star formation rate (SFR)

$$\frac{SFR}{1M_{\odot} \text{ yr}^{-1}} = \frac{L_{FIR}}{5.8 \times 10^9 L_{\odot}} \quad (2)$$

of the host galaxy using the local scalings of Kennicutt (1998b), corrected for the difference in the definition of the total infrared luminosity between Bavouzet et al. (2008) and Kennicutt (1998b). The uncertainties in the star formation rates are dominated by the uncertainties in extrapolating to the total infrared luminosity from the $8.0\mu\text{m}$ flux. Bavouzet et al. (2008) found a 38% scatter between the $8.0\mu\text{m}$ flux and L_{FIR} , while Kennicutt (1998b) found a scatter of about 30-50% between the L_{FIR} and the SFR, and also attributed it to the uncertainty in estimating the FIR luminosity from the near infrared luminosity and uncertainty in the effects of extinction (for further discussion of these uncertainties, see §6 of Caputi et al. 2007). We also used the scaling relation in Caputi et al. (2007), who argue for a different high-luminosity $L_{8.0\mu\text{m}}$ -to- L_{IR} relationship than Bavouzet et al. (2008). We found no significant difference between these two scaling relations, as the host galaxy has an $8.0\mu\text{m}$ luminosity close to the break luminosity where the Caputi et al. (2007) relation begins to differ from that of Bavouzet et al. (2008). We then used the Kennicutt (1998a) relation between UV luminosity and SFR to produce an estimate of the unobscured SFR. The Kennicutt (1998a) relation converts the UV luminosity–SFR relation of Madau et al. (1998) to a Salpeter IMF with continuous star formation. Note that the Kennicutt (1998a) relation would not apply for a starburst galaxy. The Salpeter IMF used in (Kennicutt 1998a) yields a very flat SED in the UV region used in their relation (1500–2800Å Kennicutt 1998a). This relation gives $SFR(M_{\odot} \text{ yr}^{-1}) = 1.4 \times 10^{-28} L_{\nu}(\text{ergs s}^{-1} \text{ Hz}^{-1})$. We choose to estimate L_{ν} at the mid-point of their UV spectrum (2150Å) from our template fits, which is then used to estimate the unobscured SFR. The SFRs derived from our template fits are given in Table 3, where uncertainties in the UV SFRs are dominated by uncertainties in the template fits while those in the IR SFRs are dominated by the scatter in the scaling relations. Kennicutt (1998a) note that this UV–SFR relation has the benefit of directly tracking emission from young stellar atmospheres, but would also be quite sensitive to both extinction and variation of the IMF. The Kennicutt (1998b) relation between IR luminosity and the SFR likewise assumes a Salpeter IMF with continuous star formation, but it also assumes that all of the bolometric luminosity is reprocessed in the infrared.

We combined the template models with the results of Bell et al. (2003) to estimate the

stellar mass of the host galaxy. Bell et al. (2003) assumed a universal “diet Salpeter” Initial Mass Function (IMF) and a variety of star formation histories to simulate SED templates, which they then fit to a large sample of SDSS galaxies to estimate mass-to-light ratios as a function of rest frame colors. They took these M/L ratios, in combination with the measured colors of the galaxies, to derive relationships between colors and mass-to-light ratios, $\log(M/L) = a_\lambda + (b_\lambda \times \text{color})$, as detailed in Bell et al. (2003) (Table 7). We assume a Kroupa IMF, which better represents a normal stellar population, and this introduces a -0.15 dex correction to the value of a_λ . We estimate the rest frame $(g-r)$ color and K-band luminosity from our template fits, and then use the Bell et al. (2003) K-band parameters ($a_K = -0.359$ and $b_K = 0.197$) to estimate the mass-to-light ratio. This leads to an estimated host K-band $\log(M/L) = (-0.19 \pm 0.28)(M/L)_\odot$, with uncertainties dominated by random scatter in the Bell et al. (2003) calibration and in the color derived from the template fits. The estimated rest frame $(g-r) \simeq 0.85$ color of the host puts it in the “green valley” between the star forming “blue cloud” and the “red sequence” (see e.g. Strateva et al. 2001; Blanton et al. 2003), as seen in Figure 5.

The estimated MgII and C[IV] line FWHM are 49 and 21 Å, respectively (Fohlmeister et al. 2008, Morgan, private communication). These both indicate a black hole mass of $\log(M_{BH}/M_\odot) \simeq 8.6$ based on the scalings of McClure & Jarvis (2002) for MgII and Vestergaard & Peterson (2006) for C[IV]. We have also applied the revised normalization of Onken et al. (2004) to the MgII estimate. The estimated magnification-corrected luminosity at rest-frame at 1350Å is 2.0×10^{45} erg/s based on power-law fits to the B, V, and I HST images. The uncertainties in the M_{BH} estimate are dominated by systematics, principally the 0.3 dex uncertainty typical of M_{BH} estimates from line widths and 0.15 dex from the magnification uncertainties. Nonetheless, the excellent agreement between the MgII and C[IV] mass estimates ($\log(M_{BH}/M_\odot) = 8.62$ and 8.56, respectively) is reassuring. If we estimate a black hole mass from the rest frame V-band host luminosity of $(2.07 \pm 0.03) \times 10^{43}$ ergs/s, using the relation of Gültekin et al. (2009), we find a black hole mass of $\log(M_{BH}/M_\odot) = 8.74 \pm 0.21$ that agrees well with the estimates from the line widths. Note, however, that we have no estimate of the fraction of the galactic luminosity that comes from the host’s bulge, as used in the Gültekin et al. (2009) relation, since decomposing the host galaxy into bulge and disk components is made impossible by the geometry of the lensing of the host and the high luminosity of the quasar. The Eddington luminosity for such a black hole is

$$L_{Edd} = 5.7 \times 10^{12} \left(\frac{M_{BH}}{10^{8.6} M_\odot} \right) L_\odot. \quad (3)$$

From our template models we can estimate the 0.1–24 μ m luminosity of the black hole (see Table 3). We use the 3 μ m to L_{IR} analysis from §2.6 of Gallagher et al. (2007), applied to the Boötes field AGNs to estimate a bolometric correction of $BC \simeq 1$ between this luminosity

and the bolometric luminosity (for an in depth discussion, see Assef et al. 2009).

Based on these scalings, a weighted average over the different lensed images, and assuming a Kroupa IMF, we estimate that the total (obscured plus unobscured) star formation rate is $\log(\dot{M}/M_{\odot} \text{ yr}^{-1}) = 1.21 \pm 0.26$ compared to a stellar mass of $\log(M_{\star}/M_{\odot}) = 11.09 \pm 0.28$. The uncertainties in these quantities are dominated by the scatter in the IR scaling relations. Aside from the systematic and random uncertainties in the scalings used to determine the SFR (40%, Kennicutt 1998b; Bavouzet et al. 2008) and stellar mass (26%, Bell et al. 2003), the biggest uncertainties arise from the magnification estimates. The IRAC quasar flux ratios are probably a reasonable estimate of the intrinsic flux ratios because we expect (and observe) little variability at these wavelengths, as quasar variability diminishes to longer wavelengths (Vanden Berk et al. 2004), extinction effects will be negligible, and the mid-IR emission region is too large to be strongly microlensed (e.g. Poindexter et al. 2007, on microlensing in HE 1104-1805). These IR flux ratios are $B/A \sim 0.76$, $C/A \sim 0.63$, and $D/A \sim 0.32$ compared to 0.67, 0.34, and 0.27 respectively from the Inada et al. (2008) models (Oguri, private communication). Much of this will be incorporated into the uncertainties estimated from the scatter between the various lensed images and masks. The host SED has roughly equal contributions from the E and Sbc templates and little contribution from the Irr template, independent of the image or region fit. While dust could obscure the optical/UV emission of young stars in the Irr template (see Figure 4), we would not find a good fit to the host using an obscured Irr template. Note that the inner (QSO mask) and outer (Host mask) regions of the host galaxy seem to contain a similar number of stars and have similar specific star formation rates.

We can also compare these inferences about the stars to those for the black hole. The black hole represents a mass fraction of $\log(M_{BH}/M_{\star}) = -2.49 \pm 0.28$ compared to the stars, which is marginally inconsistent with local estimates of $\log(M_{BH}/M_{\star}) = -2.85 \pm 0.12$ (Häring & Rix 2004). Our result is in better agreement with the Peng et al. (2006a) estimate that the M_{BH}/M_{\star} relation is 4_{-1}^{+2} ($\simeq 0.6$ dex) larger at $z = 1.7$ than locally (i.e. $\log(M_{BH}/M_{\star}) \simeq -2.25$). Assuming that the evolution in this relationship found by Peng et al. (2006a) is correct, the agreement of the black hole masses estimated from the line widths and the host luminosity is then a coincidence in which the effect of evolution in the relation is balanced by our over-estimation of the bulge luminosity. Finally, we note that after including our estimate of the bolometric correction, we find that $L_{BH}/L_{Edd} \simeq 0.24 \pm 0.05$, so the black hole is radiating at a significant fraction of its Eddington limit, as is typical of quasars at this epoch (e.g. Kollmeier et al. 2006). The quasar may be moderately extinguished, as we find best fits where the quasar template is reddened by $E(B - V) \simeq 0.1, 0.1, 0.15$, and 0.0 magnitudes for the A-D images, respectively.

In summary, both the host galaxy and quasar in SDSS J1004+4112 have relatively unremarkable properties. The one exception is that the host galaxy lies in the “green valley.” It is unclear from our template fits whether this galaxy is then in transition from being a star forming galaxy in the “blue cloud” to an old, red, and dead galaxy on the red sequence, or a red sequence galaxy with a recent burst of star formation that moved its color blue-ward. This galaxy’s location in the CMD is consistent with the observation of Hickox et al. (2009) that many X-ray AGN with the X-ray luminosity of SDSS J1004+4112 ($\simeq 2 \times 10^{43}$ ergs/s, Ota et al. 2006; Lamer et al. 2006) lie in the green valley, while radio AGN tend to lie on the red sequence and mid-IR selected AGN tend to lie in the blue cloud. The extreme extension of the host galaxy should also make it possible to obtain spectroscopic observations of the host galaxy, potentially allowing measurement of the dynamical mass or metallicity.

We would like to thank C. Morgan and C. Peng for their comments and help on the estimated black hole mass. We would also like to thank D. Maoz and M. Oguri for their comments. This work is based in part on observations made with the NASA/ESA *Hubble Space Telescope*. Support for programs GO-9744, 10509 and 10716 was provided by NASA through a grant from the Space Telescope Science Institute, which is operated by AURA, Inc., under NASA contract NAS5-2655. It is also based in part on observations made with the Spitzer Space Telescope, AO-20451, which is operated by the Jet Propulsion Laboratory, California Institute of Technology under a contract with NASA. Support for this program SST-20277 was provided by NASA through an award issued by JPL/Caltech. CSK is also supported by NSF grant AST-0708082.

REFERENCES

- Adelman-McCarthy, J.K., et al. 2008, ApJS, 175, 297
- Assef, R.J., et al. 2008, ApJ, 676, 286
- Assef, R.J., et al. 2009, in preparation
- Bavouzet, N., et al. 2008, arXiv:0712.0965v1 [astro-ph]
- Bell, E.F., et al. 2003, ApJ, 149, 289
- Blanton, M.R., et al. 2003, ApJ, 594, 186B
- Caputi, K.I., et al. 2007, ApJ, 660, 97C
- Di Matteo, T., et al. 2008, ApJ, 676, 33

- Fohlmeister, J., et al., 2007, ApJ, 662, 62
- Fohlmeister, J., et al. 2008, ApJ, 676, 761
- Fruchter et al. 2002, PASP, 114, 144
- Gallagher, S.C., et al. 2007, ApJ, 661, 30-37
- Gültekin, K., et al. 2009, arXiv:0903.4897
- Häring, N., Rix, H.-W. 2004, ApJ, 604, 89-92
- Hickox, R.C., et al. 2009, arxiv: 0901.4121
- Hopkins, P., et al. 2005a, ApJ, 625, 71
- Hopkins, P., et al. 2005b, ApJ, 630, 705
- Hopkins, P., Narayan, R., Hernquist, L. 2006, ApJ, 643, 641
- Hopkins, P., et al. 2006, ApJS, 163, 1
- Hopkins, P., et al. 2008, ApJS, 175, 356
- Inada, N., et al. 2003, Nature, 426, 810-812
- Inada, N., et al., 2005, PASJ, 57, 71
- Inada, N., et al. 2008, PASJ, 60, 27
- Jannuzi, B.T., Dey, A. 1999 AAS, 195, 1207J
- Kauffmann, G., Heckman, T. 2005, RSPTA, 363, 621
- Kennicutt Jr., R.C. 1998a, ARA&A, 36, 189K
- Kennicutt Jr., R.C. 1998b, ApJ, 498, 541
- Kochanek, C.S., et al. 2008, in preparation
- Kollmeier, J., et al. 2006, ApJ, 648, 128
- Lamer et al. 2006, A&A, 454, 493
- Lauer, T., et al. 2007, ApJ, 670, 249
- Lehár, J., et al. 2000, ApJ, 536, 584

- Madau, P., et al. 1998, ApJ, 498, 106
- Marconi, A., Hunt, L. 2003, ApJ, 589, 21
- McClure & Jarvis, 2002, MNRAS, 337, 109
- Oguri, M., Private communication with C.S. Kochanek 2008/07/22
- Onken, C., et al. 2004, ApJ, 615, 645
- Ota, N., et al., 2006, ApJ, 647, 215
- Peng, C.Y., et al. 2006a, ApJ, 640, 114
- Peng, C.Y., et al. 2006b, ApJ, 649, 616
- Peng, C.Y., et al. 2006c, New Astron.Rev. 50, 689-693
- Poindexter, S., et al. 2007, ApJ, 660, 146
- Sharon, K., et al. 2005, ApJ, 629, 73
- Sijacki, D., et al. 2007, MNRAS, 380, 877-900
- Strateva, I., et al. 2001, AJ, 122, 1861S
- Vanden Berk et al. 2004, ApJ, 601, 692
- Vestergaard & Peterson, 2006, ApJ, 641, 689

Table 1. Observations of SDSS J1004+4112

Program	Instrument	Filter	Date	Exposure Time (sec)	Depth
HST-9744	NICMOS/NIC2	H(F160W)	2004/04/28	2688*	21.77
	NICMOS/NIC2	H(F160W)	2004/10/09	2688	21.70
HST-10716	NICMOS/NIC2	H(F160W)	2006/10/22	2688	21.45
HST-10509	ACS/WFC	B(F435W)	2005/12/13	13378	26.26
HST-9744	ACS/WFC	V(F555W)	2004/01/28	2025	25.22
HST-10509	ACS/WFC	V(F555W)	2005/12/12	7978	26.30
HST-9744	ACS/WFC	I(F814W)	2004/04/28	2025	24.29
HST-10509	ACS/WFC	I(F814W)	2005/12/12	5360	24.41
SST-20277	IRAC	3.6–8.0 μ m	2005/12/08,	3485	20.28 ¹
			2005/12/26,		19.96 ²
			2006/11/25		18.37 ³
					17.76 ⁴

Note. — *This observation includes only images A and B. Depths are 5- σ rms noise, in Vega magnitudes, in a ~ 1 arcsec² aperture for the HST bands and ~ 4 arcsec² aperture for the SST/IRAC images. ¹ IRAC Channel 1, ² IRAC Channel 2, ³ IRAC Channel 3, ⁴ IRAC Channel 4.

Table 2. SDSS J1004+4112 Magnitudes

Filter	Date	host	Image A		host	Image B		host	Image C		Image D	
			qso	joint		qso	joint		qso	joint	qso	joint
B	2005/12/13	28.18±0.81	23.44±0.03	23.42±0.01	28.55±0.67	23.24±0.03	23.22±0.01	26.43±0.86	22.67±0.57	22.64±0.45	22.87±0.36	
V	2004/01/28	27.93±1.12	23.36±0.15	23.34±0.13	27.39±1.18	23.29±0.15	23.26±0.13	26.34±1.25	22.65±0.15	22.61±0.15	22.41±0.14	
V	2005/12/12	27.76±1.11	23.29±0.10	23.27±0.08	27.59±1.19	23.27±0.11	23.24±0.08	26.69±1.09	22.62±0.11	22.59±0.08	22.73±0.08	
I	2004/04/28	25.52±0.97	22.30±0.16	22.26±0.16	25.39±0.81	22.16±0.16	22.11±0.15	24.73±0.65	21.48±0.16	21.41±0.16	21.86±0.16	
I	2005/12/12	25.78±0.73	22.42±0.10	22.36±0.04	25.57±0.72	22.27±0.12	22.21±0.04	24.65±0.61	21.83±0.24	21.76±0.19	21.64±0.03	
H	2004/04/28	22.43±0.23	21.26±0.10	21.02±0.11	22.36±0.14	21.09±0.11	20.86±0.11	
H	2004/10/09	22.41±0.41	20.93±0.08	20.66±0.13	21.89±0.40	20.88±0.09	20.47±0.14	21.36±0.40	20.05±0.10	19.64±0.15	19.85±0.13	
H	2006/10/22	22.38±0.15	21.16±0.10	20.87±0.09	21.94±0.33	20.86±0.10	20.48±0.13	21.79±0.37	20.53±0.08	20.21±0.11	20.20±0.10	
3.6 μ m	2005/12/08	19.94±0.33	18.69±0.01	18.30±0.05	19.42±0.21	18.60±0.03	18.07±0.09	19.05±0.58	18.11±0.04	17.64±0.16	17.79±0.17	
3.6 μ m	2005/12/26	19.80±0.17	18.72±0.02	18.29±0.07	19.41±0.33	18.65±0.02	18.10±0.10	19.18±0.34	18.05±0.02	17.62±0.06	17.77±0.04	
3.6 μ m	2006/11/25	19.80±0.22	18.86±0.06	18.42±0.10	19.37±0.32	18.67±0.06	18.10±0.07	18.96±0.22	18.07±0.06	17.58±0.08	17.71±0.06	
4.5 μ m	2005/12/08	19.12±0.23	17.87±0.01	17.46±0.06	18.90±0.11	17.74±0.02	17.32±0.03	18.14±0.07	17.36±0.02	16.83±0.03	17.07±0.04	
4.5 μ m	2005/12/26	19.01±0.22	17.92±0.02	17.47±0.03	18.86±0.08	17.81±0.02	17.36±0.03	18.16±0.15	17.34±0.02	16.81±0.07	17.08±0.02	
4.5 μ m	2006/11/25	19.04±0.22	18.01±0.05	17.59±0.05	18.89±0.04	17.85±0.05	17.43±0.05	18.07±0.21	17.41±0.05	16.87±0.06	16.99±0.05	
5.8 μ m	2005/12/08	18.92±0.32	17.03±0.01	16.71±0.03	18.60±0.15	16.96±0.02	16.62±0.06	18.09±0.23	16.49±0.01	16.15±0.02	16.40±0.03	
5.8 μ m	2005/12/26	19.08±0.40	17.06±0.01	16.76±0.04	18.87±0.18	16.96±0.01	16.65±0.03	18.15±0.13	16.46±0.01	16.12±0.02	16.41±0.02	
5.8 μ m	2006/11/25	18.95±0.40	17.12±0.04	16.90±0.06	18.77±0.22	16.91±0.04	16.70±0.05	18.04±0.15	16.42±0.04	16.22±0.07	16.35±0.04	
8.0 μ m	2005/12/08	18.53±0.17	15.93±0.01	15.89±0.01	18.27±0.48	15.85±0.01	15.80±0.02	17.96±0.32	15.31±0.01	15.38±0.01	15.73±0.02	
8.0 μ m	2005/12/26	18.51±0.18	16.07±0.01	15.88±0.02	18.45±0.30	16.00±0.01	15.85±0.03	17.87±0.14	15.49±0.01	15.38±0.01	15.71±0.02	
8.0 μ m	2006/11/25	18.46±0.08	15.87±0.03	16.02±0.03	18.27±0.23	15.73±0.03	15.91±0.04	17.78±0.09	15.11±0.03	15.45±0.03	15.66±0.04	

Note. — These are Vega magnitudes corrected for magnification by the lens based on the models of Inada et al. (2008, Oguri private communication). The fluxes in the QSO mask contain a portion of the host galaxy. The QSO and joint fluxes are adjusted to account for time-dependent variability in the quasar using corrections from the monitoring data of Fohlmeister et al. (2008). The 2004/04/28 NICMOS H-band observation included only images A and B.

Table 3. Magnification Corrected Properties

Image	Mask	E	Sbc	Irr	QSO	SFR _{IR}	SFR _{UV}	(M/L) _K	M _★
		(Luminosity in units of 10 ¹⁰ L _⊙)				(M _⊙ yr ⁻¹)	(M _⊙ yr ⁻¹)	Solar Units	(10 ¹⁰ M _⊙)
A	host	1.05±0.64	2.84±0.95	0.038±0.120	≡0	8.8±4.0	0.36 ± 0.14	0.605±0.100	4.3±0.7
	qso	1.35±0.01	1.93±0.01	0.104±0.001	145.6±0.2	6.5±2.4	0.19 ± 0.01	0.597±0.105	1.9±0.4
	joint	2.87±0.06	4.09±0.09	0.219±0.005	125.7±0.7	12.1±4.5	0.80 ± 0.02	0.578±0.100	8.4±1.0
B	host	2.02±1.04	1.86±1.72	0.049±0.133	≡0	6.3±5.1	0.29 ± 0.11	0.612±0.100	4.9±0.6
	qso	1.40±0.01	1.99±0.01	0.107±0.001	167.0±0.2	6.7±2.5	0.53 ± 0.02	0.591±0.101	5.6±0.8
	joint	4.69±0.06	6.67±0.09	0.358±0.005	108.9±0.8	18.2±6.8	1.30 ± 0.02	0.575±0.100	13.6±1.5
C	host	4.06±1.49	2.57±2.25	0.685±0.448	≡0	8.9±6.4	1.22 ± 0.54	0.610±0.100	9.0±1.4
	qso	3.00±0.02	4.26±0.02	0.229±0.010	250.7±0.6	12.6±4.7	0.70 ± 0.01	0.595±0.103	7.3±0.8
	joint	8.57±0.17	12.19±0.24	0.655±0.013	166.6±1.7	30.1±11.1	2.38 ± 0.05	0.590±0.101	24.9±2.8
D	joint	7.42±0.07	10.55±0.10	0.567±0.005	126.2±1.4	26.7±9.9	2.06 ± 0.02	0.621±0.102	21.6±2.2
Avg	host	1.64±0.51	2.60±0.78	0.067±0.087	≡0	8.1±2.8	0.35 ± 0.52	0.609±0.058	5.1±0.5
	qso	1.81±0.03	1.96±0.03	0.165±0.003	155.0±0.6	4.8±1.0	0.44 ± 0.26	0.594±0.059	3.4±0.3
	joint	5.54±0.04	6.01±0.04	0.505±0.003	124.0±0.5	15.0±3.0	1.39 ± 0.72	0.591±0.050	12.3±0.7

Note. — Contribution of each template to the SED. These are corrected for magnification based on the models of Inada et al. (2008, Oguri private communication). The star formation rates (SFR) and stellar mass are estimated as described in §3. Note that the average values at the bottom of the table (Avg) are uncertainty weighted averages of the corresponding values for the individual components.

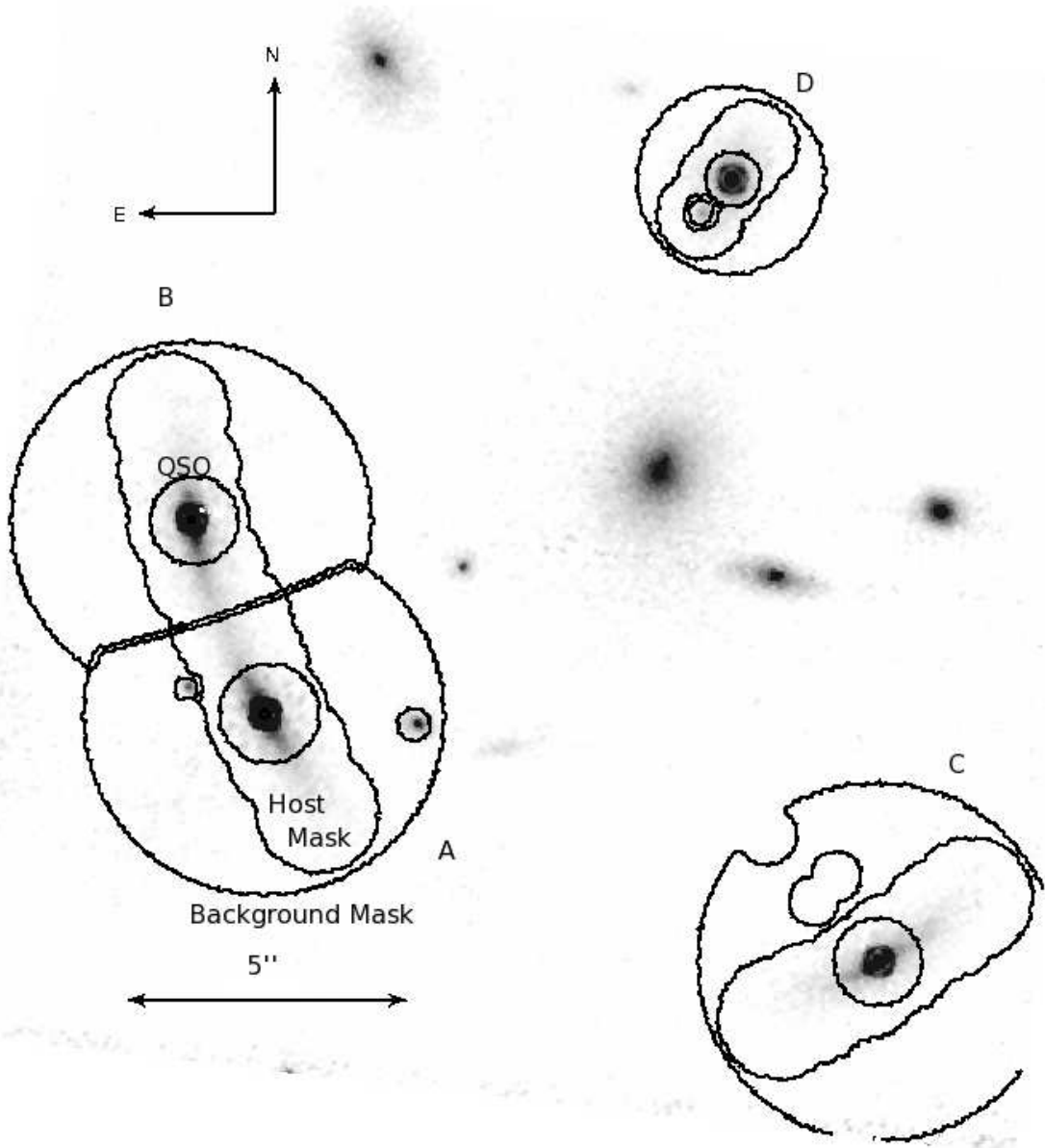


Fig. 1.— NICMOS/NIC2 H-band (F160W) image of SDSS J1004+4112 with mask outlines denoted by the solid black lines. The host galaxy is clearly seen stretched out from beneath the peak of the QSO. For image D we only use the joint mask.

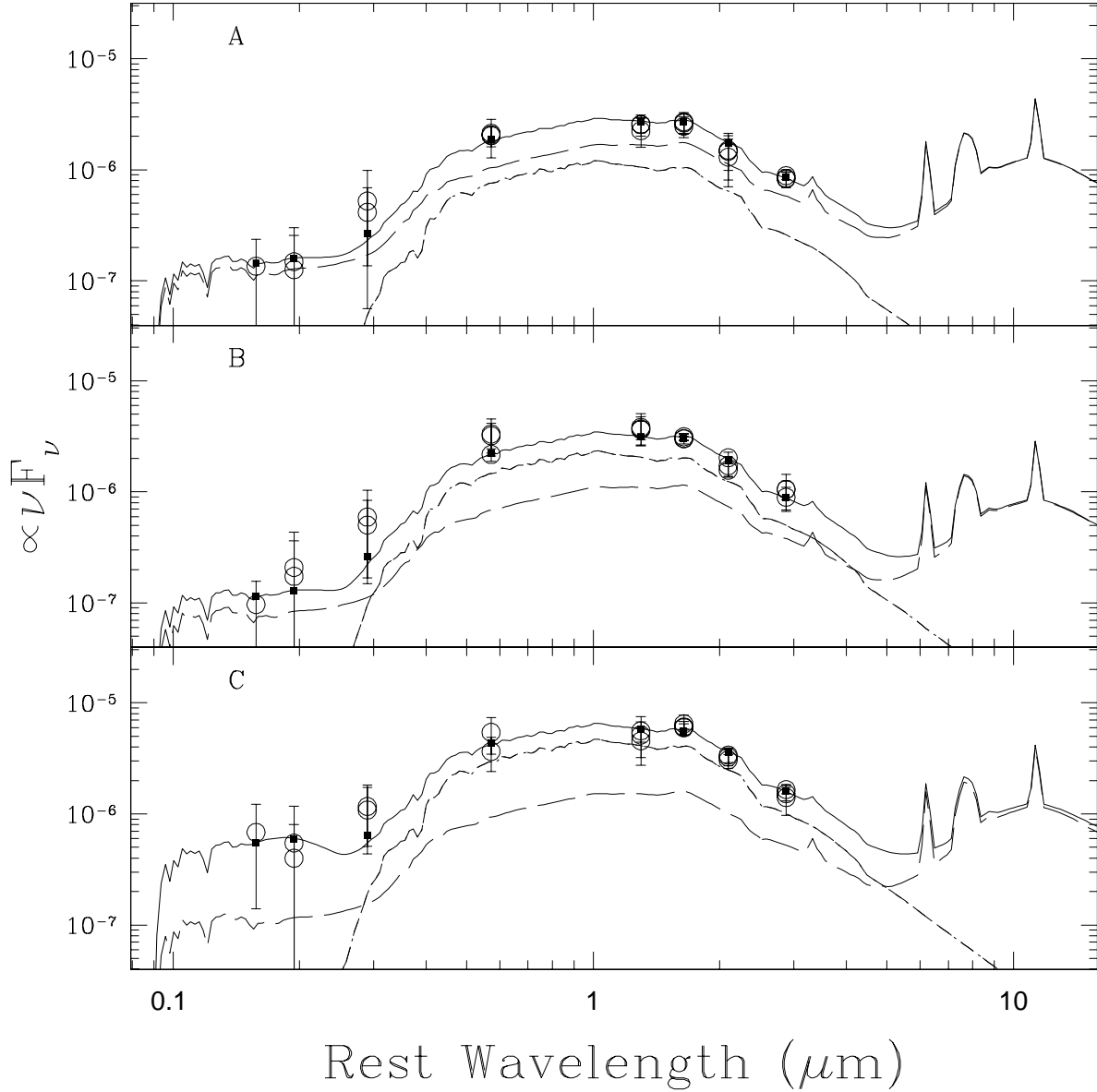


Fig. 2.— Host mask spectral energy distribution for images A (Top), B (Middle), and C (Bottom). Observation bands are, from left to right, ACS/WFC B(F435W), V(F555W), I(F814W), NICMOS/NIC2 H(F160W), IRAC 3.6, 4.5, 5.8, and 8.0 μm . The results for all observation epochs are shown. The solid, dot-dashed, long-dashed, and short-dashed lines correspond to the total SED and the contribution from the E, Sbc, and Irr templates respectively. The open circles are the measured fluxes while the closed squares are the best fit value given the template fits. The contribution from the Irr template is too small to be seen on this scale. The SEDs are corrected for magnification by the lens based on the models of Inada et al. (2008, Oguri private communication).

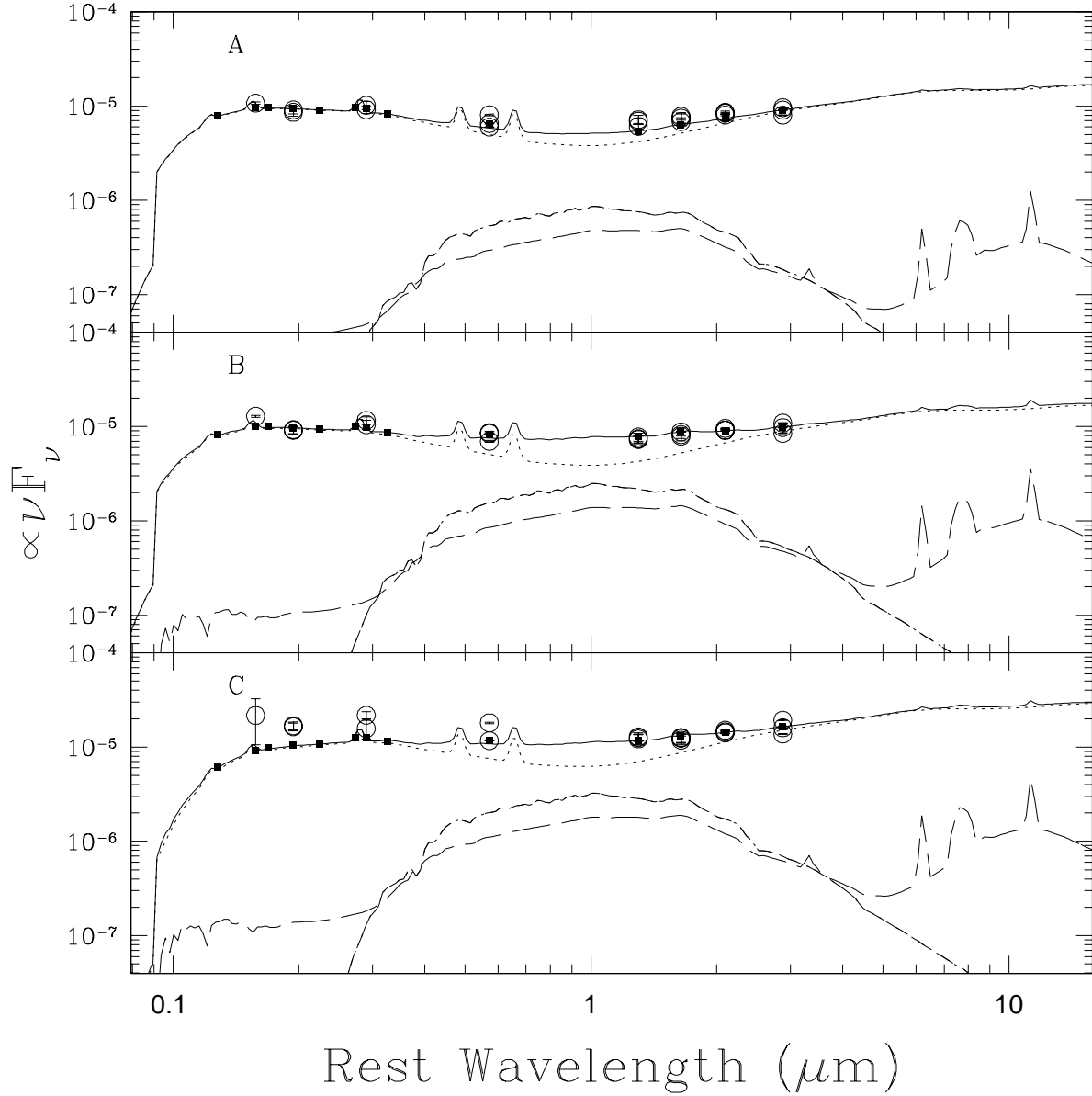


Fig. 3.— QSO mask spectral energy distribution for images A (Top), B (Middle), and C (Bottom). The galaxy templates and data points are represented as described in Figure 2 while the dotted line shows the QSO template and the solid line shows the sum of all templates. The contribution from the Irr template is too small to be seen on this scale. The changes in the optical continuum slope are due to the variations in the QSO extinction estimates.

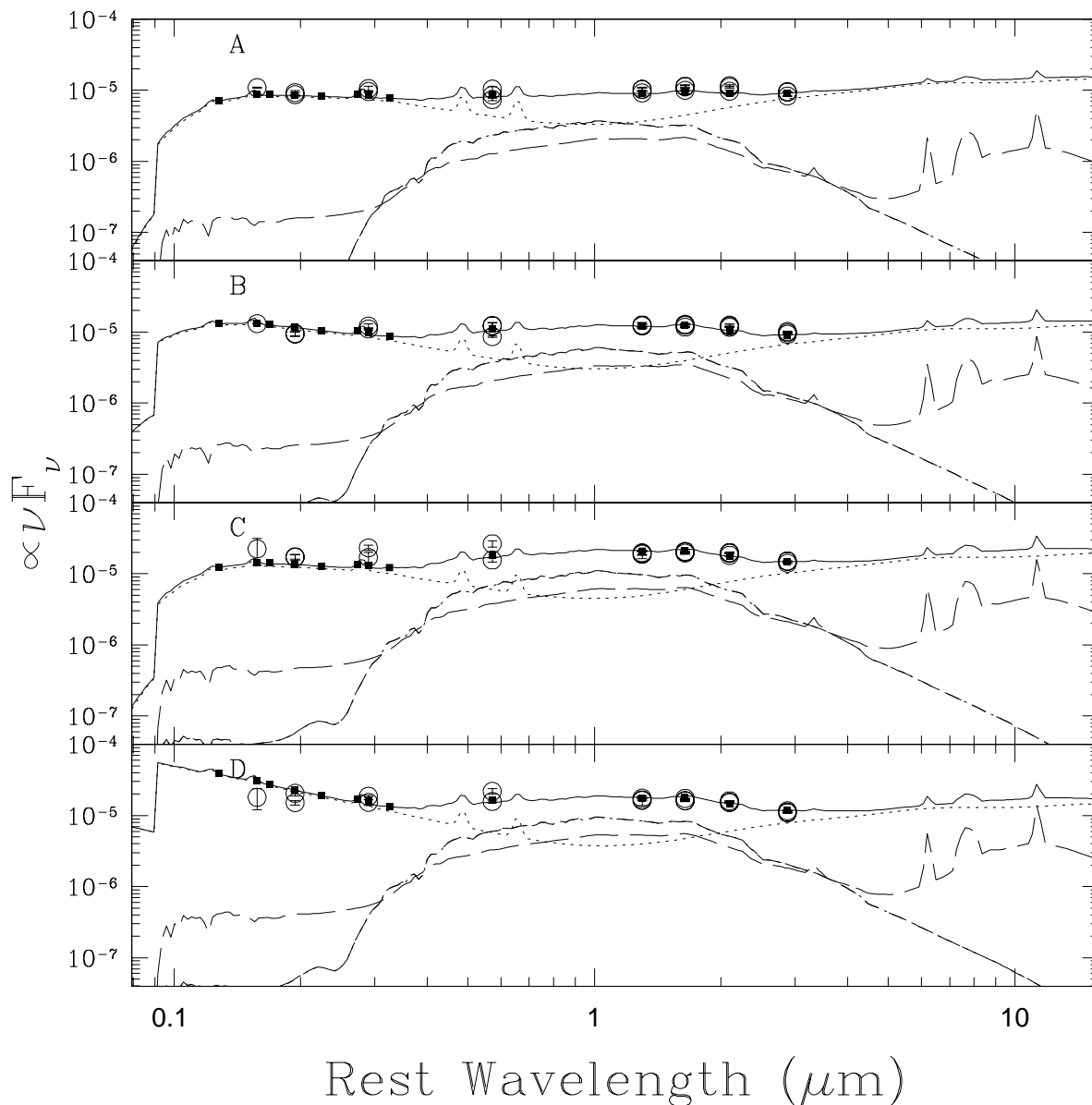


Fig. 4.— Joint mask (QSO + Host) spectral energy distribution for images A (Top), B (Top Middle), C (Bottom Middle), and D (Bottom). The components are as described in Figs. 2 and 3. The contribution from the Irr template is too small to be seen on this scale. Note that the template models show some variation in the amount of extinction accounted for in the various images.

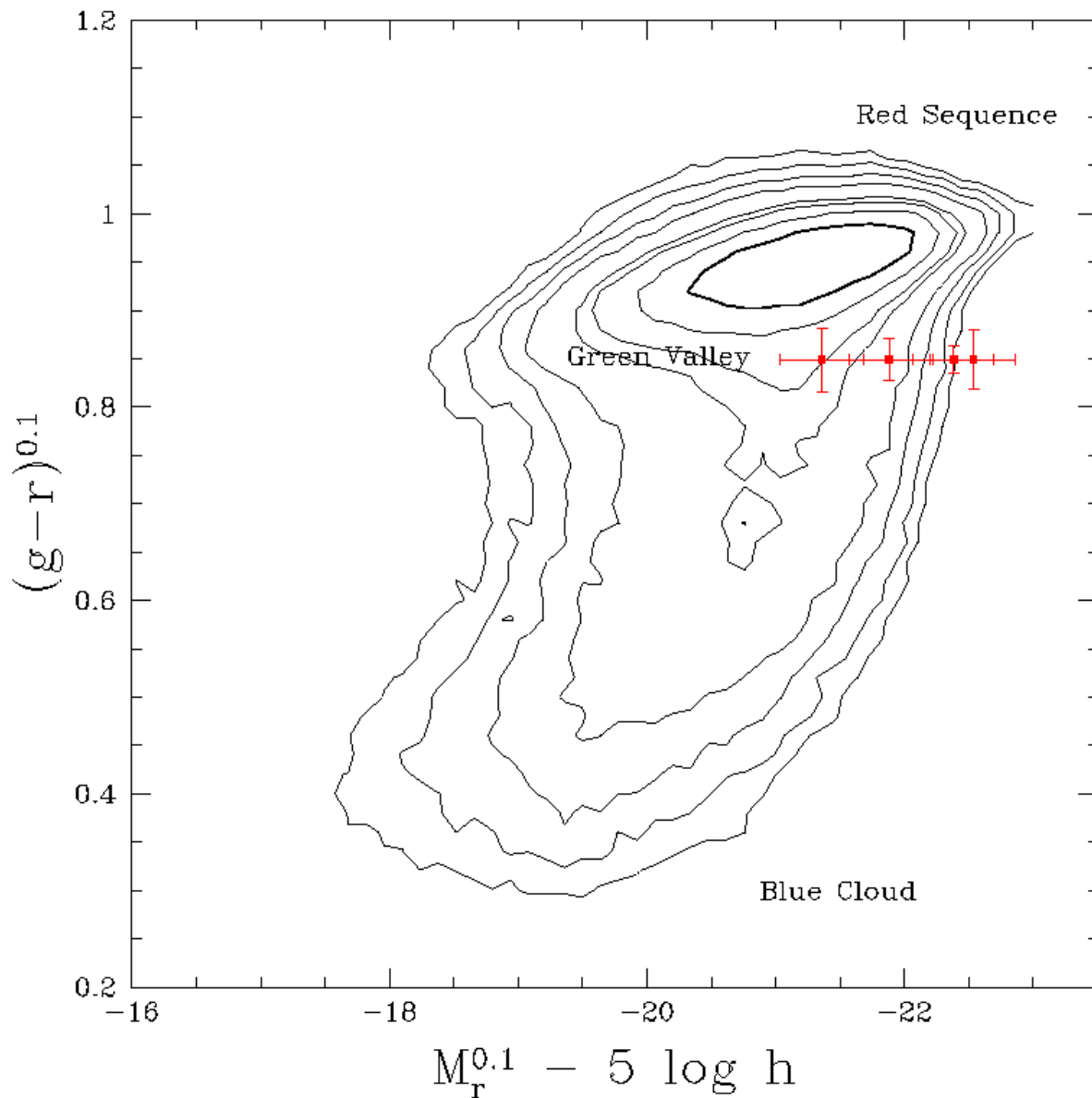


Fig. 5.— Color-magnitude diagram of SDSS galaxies from the SDSS Data Release 6 (Adelman-McCarthy et al. 2008) with the points for the four images of SDSS J1004+4112 in red. The systematic effects on the luminosity from estimates of the magnification for each lensed image is clearly seen from the similarity in color as compared to the factor of $\simeq 2$ differences in the estimates of the magnification-corrected luminosity.